CrossMark

Tandem laser ablation synthesis in solution-galvanic replacement reaction (LASiS-GRR) for the production of PtCo nanoalloys as oxygen reduction electrocatalysts

Sheng Hu [b, d], Mengkun Tian [c], Erick L. Ribeiro [b, d], Gerd Duscher [c],
Dibyendu Mukherjee [a, b, d, *]

[a] Department of Mechanical, Aerospace, and Biomedical Engineering, University of Tennessee, Knoxville, TN, USA
[b] Department of Chemical and Biomolecular Engineering, University of Tennessee, Knoxville, TN, USA
[c] Department of Material Science and Engineering, University of Tennessee, Knoxville, TN, USA
[d] Sustainable Energy Education and Research Center (SEERC), University of Tennessee, Knoxville, TN, USA

HIGHLIGHTS

- Tandem LASiS-GRR is used to synthesize PtCo nanoalloys (NAs) as electrocatalysts.
- Size and degrees of alloying are tuned by Pt salt concentrations and pH conditions.
- EELS mapping reveals Pt-rich shell on PtCo alloyed core.
- NAs with Co molar ratio~22.1% indicate superior ORR activities in acid electrolytes.
- A mechanistic picture for LASiS-GRR controlling PtCo alloying process is proposed.

GRAPHICAL ABSTRACT
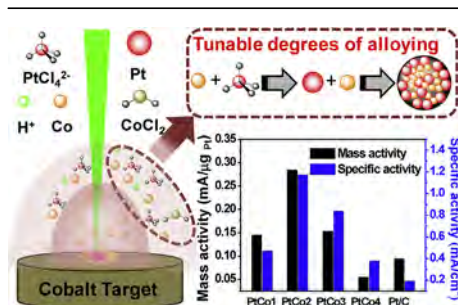
ARTICLE INFO

ABSTRACT

We have developed tandem laser ablation synthesis in solution-galvanic replacement reaction (LASiS-GRR) technique as a facile, green yet, efficient route to synthesize spherical PtCo NAs with varied sizes, compositions and degrees of alloying. The transformative concept here is the ability to design these nanostructured alloys by tuning the high-energy physico-chemical conditions emerging from liquid-confined, laser-induced plasma, and the solution-phase reaction pathways dictated by pH conditions and precursor salt concentrations. The resultant NAs exhibit uniformly alloyed cores with a Pt-rich shell of a few nanometers, as demonstrated by the electron energy loss spectroscopy (EELS) mapping. Such core—shell structure along with high degrees of alloying in these PtCo NAs promote their outstanding electrocatalytic ORR activities in acid electrolytes. Specifically, compared to commercial Pt/C catalysts, the PtCo NAs with Co molar ratio of 22.1% indicate a c.a. 3 and 6-fold increase in mass and specific activities respectively. Such enhanced ORR activities are attributed to the efficacy of tandem LASiS-GRR route to rationally tune size distributions/compositional ratios and alloying degrees of the NAs

---

 * Corresponding author. Department of Mechanical, Aerospace, and Biomedical Engineering, University of Tennessee, Knoxville, TN, USA.
    E-mail address: dmukherj@utk.edu (D. Mukherjee).

without the use of any surfactants or reducing agents that are otherwise indispensable in chemical synthesis methods, but harmful for catalytic performances.

1. Introduction

The energetically expensive oxygen reduction reactions (ORR) at the cathode have been the rate determining step and hence, a severe hindrance to efficient and clean electrochemical energy conversions in low-temperature proton exchange membrane fuel cells (PEMFCs) [1–7]. To promote the ORR activities, Pt based nanocatalysts have largely been used for most commercial applications [6,8–10]. Yet, the cost of precious metal based catalysts added to the lack of stability and durability of Pt under the highly corrosive and acidic conditions of fuel cell operations have prompted a large volume of research in recent years geared towards the development of transition metal based alloys and/or, intermetallic materials with low Pt-loading [11–16]. Specifically, recent U.S. DRIVE fuel cell technical roadmap has established the 2020 target for the total loading of Pt group metals (PGM) to be ~0.125 mg/cm^2 electrode area for PEMFC electrocatalysts [17]. To this end, alloyed nanocatalysts have gained tremendous research interest in the past decade due to their unique geometric and/or electronic characteristics that dramatically enhance their catalytic activities, while reducing the net PGM content [18–24]. Alloying Pt with 3-d transition metals such as Co, Ni, Fe, etc have been found to effectively shrink the lattice constant (geometric effect) and downshift the d-band center (electronic effect), resulting in a moderate oxygen binding energy (eV) and consequently improved specific and mass activities for electrocatalytic ORR processes [3,19,20,25–28].

Among the aforementioned Pt based nanoalloys, PtCo system has attracted the most attention due to its relatively higher activity and stability for the ORR process [5,29–36]. The nominal Pt:Co ratio as well as the degree of alloying in these nanocatalysts play a critical role in tuning the nanoscale crystalline structures and band structures which in turn dictate the aforementioned geometric and electronic effects responsible for tailoring their ORR catalytic activities [4,37,38,30]. Conventional PtCo alloys were usually prepared by simultaneous reduction of cobalt salts (e.g., $Co(NO_3)_2$, $CoCl_2$) and platinum precursors ($Pt(acac)_2$, K_2PtCl_4, H_2PtCl_4) in either organic or aqueous conditions, and almost always involve the use of external and indispensible stabilizing agents (CTAB, PVP, oleylamine etc.) [1,37,34]. Recently, a wide range of synthesis techniques have been developed that include impregnation [30], solvothermal method [39], tandem decomposition and chemical reduction [22], polyol method [40], reverse micelle method [41], replacement reaction [42], etc. Yet, most of those synthesis techniques involve wet chemical routes that require intricate steps and even these techniques inevitably use harsh unwanted chemicals in the form of surfactants and/or, stabilizing agents. These organic residues on the NP surface are detrimental to their interfacial catalytic properties and eventually, systematic removal of those organic encapsulations from these alloyed/intermetallic NPs becomes a challenging and critical step in itself for large-scale production of nanocatalysts. Besides, a fine control of the Pt:Co atomic ratios and alloying degrees for systematic synthesis of a wide range of nanocatalysts still remains elusive in most of these techniques, thereby restricting the application of these ORR catalysts to only limited environmental conditions [5,41,38,40,43]. As a consequence, clean synthesis of PtM alloyed NPs that allows precise

construction of inter-atomic structure and extent of alloying in a facile, cheap, and reproducible manner is imperative.

To this end, we previously reported laser ablation synthesis in solution-galvanic replacement reaction (LASiS-GRR) as a green synthesis technique for manufacturing PtCo/CoO$_x$ nanocomposites (NCs) as excellent bifunctional catalysts for both ORR and oxygen evolution reaction (OER) in alkaline media [61]. The current work builds on a modified LASiS-GRR technique to synthesize pure PtCo alloys (no CoO$_x$ NPs) that exhibit excellent ORR activities in acid electrolyte solutions. Specifically, LASiS has attracted great interests in the past decade as a clean, yet efficient synthesis technique for manufacturing metal/metal oxide nanomaterials of various sizes and shapes [44–49], indicating our recent work on CoO$_x$/Co(OH)$_2$ synthesis. In principle, LASiS involves a liquid-confined plasma plume expanding with extremely high temperatures and pressures (c.a. 10^3 K and 10^9 Pa respectively) [50] that thermally vaporizes a metal target and initiates ultrafast propagation of cavitation bubbles. Typically, these cavitation bubbles contain the nucleated seeding NPs that finally undergo rapid collisional quenching at the bubble–liquid interface [45,50–54], while initiating simultaneous chemical reduction reactions with the solutions phase precursors/species. Here, the charge screening effects inherent to the plasma promote a uniform dispersion of the colloidal NPs in solution-phase without the need for any surfactants/stabilizing agents that are, as also discussed earlier, potentially harmful for surface catalytic activities [55]. The current work involves the LASiS-GRR process in the presence of PtCl$_4$$^{2-}$ ions as the solution-phase metal precursors. In such a setup, seeding Co NPs from within the cavitation bubble go through two competing reactions at the liquid front, namely: 1. reactions with the solution-phase H$^+$ ions from water and/or, 2. GRR with PtCl$_4$$^{2-}$ ions from the precursor salt. The latter results in the formation of Pt NPs that rapidly alloy with the remaining seeding Co NPs in the solution to form the NAs. In the results presented here, the aforementioned reaction pathways are systematically driven by tuning the initial Pt salt concentrations and solution phase pH to synthesize Pt–Co nanoalloys with controllable size, atomic ratio and alloying degrees. In turn, we investigate the structure-property relations in a wide range of as-synthesized PtCo NAs by establishing the underlying relationship between their alloyed structures, compositions and ORR activities.

2. Experimental

2.1. Synthesis of PtCo alloy NPs

Co pellets were bought from Kurt J. Lesker (99.95% purity, 1/4″ diameter × 1/4″ height) and Potassium tetrachloroplatinate (II) (K_2PtCl_4) (>99.9%) were bought from Sigma–Aldrich. All LASiS-GRR experiments were carried out in an in-house built cell equipped with facilities for simultaneous injection of metal salt solutions, temperature control as well as ultrasonication, as depicted in the supporting information (Fig. S1) and discussed in details in our earlier work [56]. For the synthesis of PtCo nanoalloys via tandem LASiS-GRR technique at neutral conditions, four different concentrations of K_2PtCl_4 salt solutions (namely 125, 250, 375 and 500 mg/l) in de-ionized water (DI-water; Purity = 99.9%; Conductivity = 18.2 MΩ/cm at 25 °C) were used along with the

respective ablation times of 4, 7, 13 and 20 min. The ablation times were chosen for ~60% reduction of initial K_2PtCl_4 precursors in each of the cases (as determined from ICP-OES measurements). Thereafter, each of the freshly prepared K_2PtCl_4 solution was transferred into the LASiS cell through the injection unit, bubbled with N_2 for 30 min. The Co pellet was then ablated in those O_2-free K_2PtCl_4 solutions using unfocused 1064 nm laser (330 mJ/pulse, 10 Hz) for various time. Right after ablation, the pH of the produced colloidal solution was adjusted to 2 by adding HCl (1 M) followed by aging in darkness for 20 h. Finally, the PtCo NPs were collected by centrifuging at 4700 rpm for 15 min and decanted after washing with DI-water for two times. For LASiS-GRR at different pH, KOH and HCl were used for preparing K_2PtCl_4 solutions (250 mg/l) in alkaline (pH = 11) and acid (pH = 2) conditions respectively. The synthesis and post treatment procedures were identical to the ones carried out for the neutral condition. Besides, all the LASiS-GRR experiments mentioned above were carried out at room temperature with simultaneous probe ultrasonication. The Co target was rotated by a stepper motor at a uniform speed of 0.3 rpm during ablation.

2.2. Characterization

A Zeiss Libra 200MC monochromated transmission electron microscope (TEM) was used with an accelerating voltage of 200 kV for regular TEM characterizations along with selected area electron diffraction (SAED) and high resolution transmission electron microscopy (HRTEM) imaging. Large-scale & small-scale elemental mappings are obtained from energy dispersive X-ray spectroscopy (EDX) and electron energy-loss spectroscopy (EELS) analysis. Information limitation of HRTEM image is 0.1 nm. Spatial resolution of the STEM image is 0.4 nm. Resolution of EELS spectrum with monochromator is 0.1 eV measured at full width of half maximum (FWHM) of zero-loss peak in the vacuum. Inductively coupled plasma optical emission spectroscopy (ICP-OES) (Perkin Elmer, Optima 4300 DV) was used to measure the concentration for both Pt and Co NPs. Standard cobalt dichloride solution ($\geq$99%) and K_2PtCl_4 solution (>99.9%) were used for calibration. X-ray diffraction (XRD) was carried out on a Phillips X'Pert-Pro diffractometer equipped with a Cu Ka source at 40 kV and 20 mA. The mean crystal sizes of the NAs were calculated according to Scherrer equation:

$$d = \frac{0.9\lambda}{\beta \cos \theta}$$

where d is the mean crystal size, λ is wavelength of the X-ray, β is the line broadening at half the maximum intensity (FWHM), θ is the Bragg angle.

The Co atomic fractions in the alloy (x) were evaluated using the Vegard's law,

$$x = \left[\frac{a - a_0}{a_s - a_0}\right] \cdot x_s$$

where a_o and a_s are the lattice parameters of Pt (0.393 nm) and Pt_3Co (0.383 nm), and x_s is the Co atomic fraction (0.25) in the Pt_3Co catalyst. The degree of alloy, i.e. the alloyed Co (Co_{al}) to total Co in the catalyst (Co_{tot}) ratio can then be expressed by:

$$\frac{Co_{al}}{Co_{tot}} = \frac{xPt_{ICP}}{(1 - x)Co_{ICP}}$$

where Pt_{ICP} and Co_{ICP} are the integral atomic ratios of Pt and Co from ICP-OES measurements, respectively.

2.3. Electrochemical tests

The rotating disk electrode (RDE) setup was bought from Pine instrument company, LLC. A conventional, three-compartment electrochemical cell comprising of a saturated double junction Ag/AgCl electrode as the reference electrode, a glassy carbon RDE with diameter of 5 mm as the working electrode, and a platinum coil as the counter electrode. All electrochemistry (EC) tests were carried out at room temperature in 0.1 M $HClO_4$ solution with the reference electrode calibrated in response to the reversible hydrogen electrode (RHE). 20% Pt/C from BASF was used as the standard catalyst for comparison. For ORR tests, synthesized NPs were first mixed with Vulcan XC-72 carbon black (CB) powder (particle size 20–40 nm, procured from Cabot Company) in aqueous solution with a weight ratio of 1:3 (NP: CB). After 2 h of ultrasonication, the slurry was stirred for 24 h and then, completely dried in vacuum at 80 °C. Thereafter, the catalyst ink was prepared by suspending 2 mg of the dried mixture in 1 mL ethanol and 5 μl of 5 wt% Nafion solution (Sigma–Aldrich, density 0.874 g/mL) via 30 min of ultrasonication. For preparing the working electrode, rotational drying method was applied wherein, 10 μL of the prepared catalyst ink was casted on the surface of the glassy carbon electrode (GCE) that was inversely placed on the RDE setup and rotated at 700 rpm for 5 min. The NP loading density was calculated to be 25 μg/cm^2. Cyclic voltammetry was conducted over a potential range from +0.05 V to +1.00 V at a scan rate of 50 mV/s after pre-scan the same potential range at 100 mV/s for 50 cycles. The ORR polarization curves were obtained by sweeping the potential from +0.05 to +1.02 V at a scan rate of 5 mV/s and a rotation rate of 1600 rpm. The dynamics of the electron transfer process in ORR were analyzed through the rotating disk voltammetry (RDV) at different speeds (ranging between 400 and 2200 rpm) based on the Koutecky–Levich (KL) equation:

$$\frac{1}{J} = \frac{1}{J_K} + \frac{1}{J_L} = \frac{1}{J_K} + \frac{1}{B\omega^{1/2}}$$

$$J_K = nFkC_0; B = 0.62nFC_0D_0^{2/3}\nu^{-1/6}$$

where J, J_K and J_L are the measured, kinetic and diffusion limiting current densities respectively, n is the electron transfer number, F is the Faraday constant (96 485 C*mol^{-1}), C_o and D_o are the dissolved O_2 concentration the O_2 diffusion coefficient in the electrolyte respectively, ν is the electrode rotation rate in rpm. Tafel plots are generated using the kinetic current J_K as determined from:

$$J_K = \frac{J * J_L}{J_L - J}$$

The electrochemical surface area (ECSA) was determined by the hydrogen desorption area in the CV curve between 0.05 and 0.4 V vs. RHE based on the following equation:

$$ECSA = \frac{Q_H}{m \times q_H}$$

where Q_H is the charge for hydrogen desorption, m is the loading amount of metal in the electrode, and q_H is the charge required for monolayer desorption of hydrogen on Pt (210 μC/cm^2).

3. Results and discussion

3.1. Synthesis and characterization of PtCo NAs

3.1.1. PtCo NAs synthesized with different Pt salt concentrations

The PtCo NA samples of PtCo-1, PtCo-2, PtCo-3, and PtCo-4, as synthesized by LASiS-GRR for various K_2PtCl_4 concentrations and ablation times (as described in the methods section), are depicted in the TEM images in Fig. 1 along with the corresponding SAED patterns (inset). It is noted here that the initial products from the LASiS-GRR synthesis were found to be alloyed PtCo NPs embedded in sponge shaped CoO_x matrices, as discussed in details in our recent work [61] and shown in the supporting information (Fig. S2a&c). As mentioned in the methods section, post-treatment of the as-synthesized $PtCo/CoO_x$ nanocomposite suspensions with HCl acid solutions at pH2 for 20 h led to the complete removed of all CoO_x matrices leaving behind the pure spherical PtCo nanoalloys (NAs) (see Fig. S2b in supporting information). These spherical PtCo NAs are found to exhibit clean PtCo characteristic diffraction rings as seen from SAED patterns in Fig. 3 insets (see Fig. S2d for enlarged images). The particles are largely found to be spherical due to the surface atom reconstruction induced by laser irradiation [57]. TEM images in Fig. 1a–d also indicate a systematic increase in the average particle sizes between the samples PtCo-1 and PtCo-4. Detailed mean crystallite sizes, as estimated from XRD data, are found to be ~3.16, 4.7, 9.00 and 10.06 nm for PtCo-1, PtCo-2, PtCo-3 and PtCo-4 samples respectively (Table 1). Mean crystallite sizes are
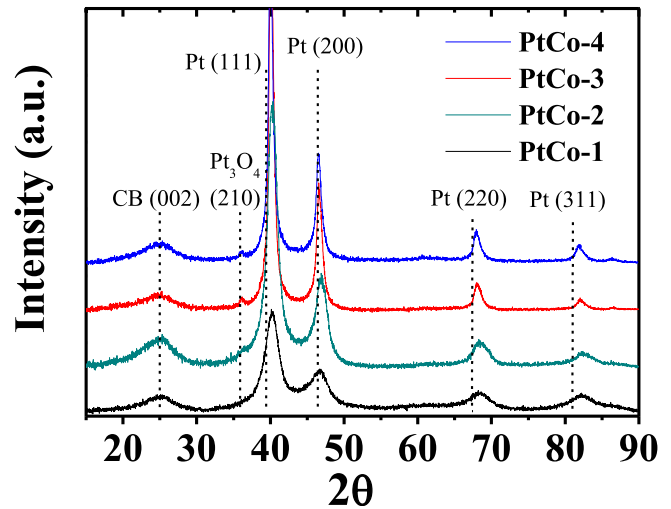
Fig. 2. Comparison of XRD patterns for various PtCo NAs synthesized at different initial K_2PtCl_4 concentrations and ablation times. The black dashed lines mark the standard peak positions for the respective labeled species.

calculated from the full width half maximum (FWHM) of the PtCo (111) peaks in the XRD patterns (Fig. 2) by applying the Scherrer equation (described in details in the methods section). The augmentation of mean particle sizes with higher initial $[Pt^{2+}]$ is due
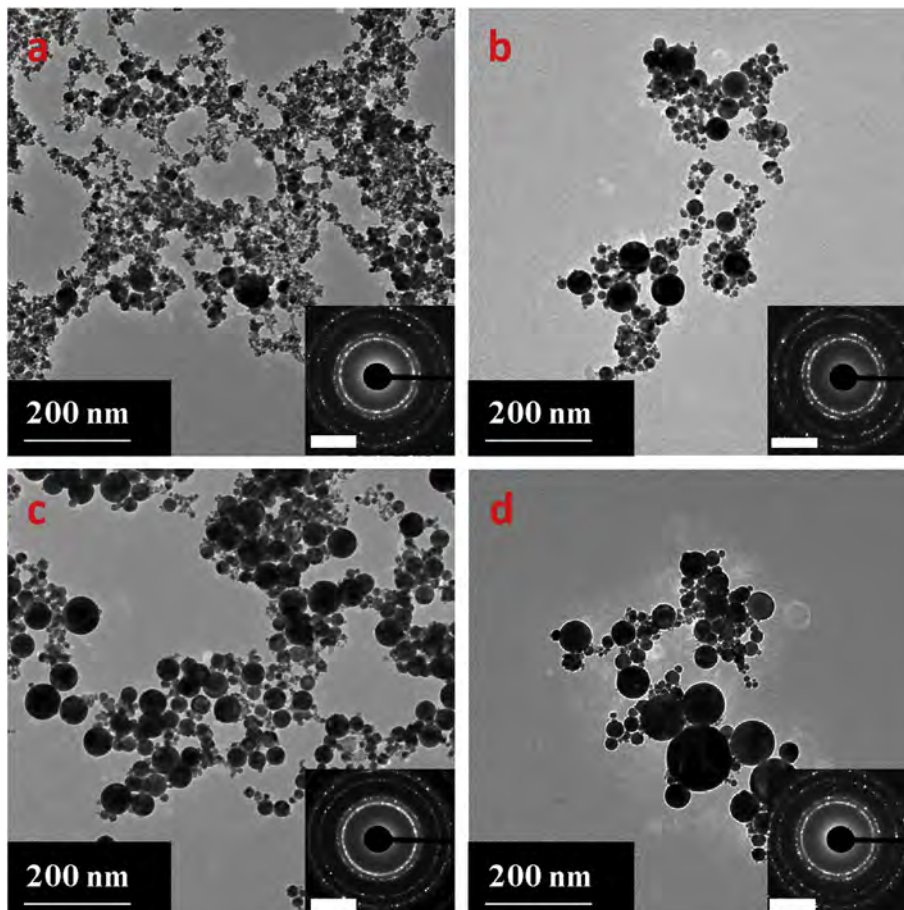
Fig. 1. a–d. TEM images along with the corresponding SAED patterns (insets) for the PtCo NAs: **a.** PtCo-1; **b.** PtCo-2; **c.** PtCo-3; **d.** PtCo-4 synthesized via LASiS-GRR at different initial K_2PtCl_4 concentrations (125 mg/l, 250 mg/l, 375 mg/l, 500 mg/l) with the respective ablation times of 4 min, 7 min, 13 min, 20 min. The scale bar in for SAED patterns is 5 (1/nm).
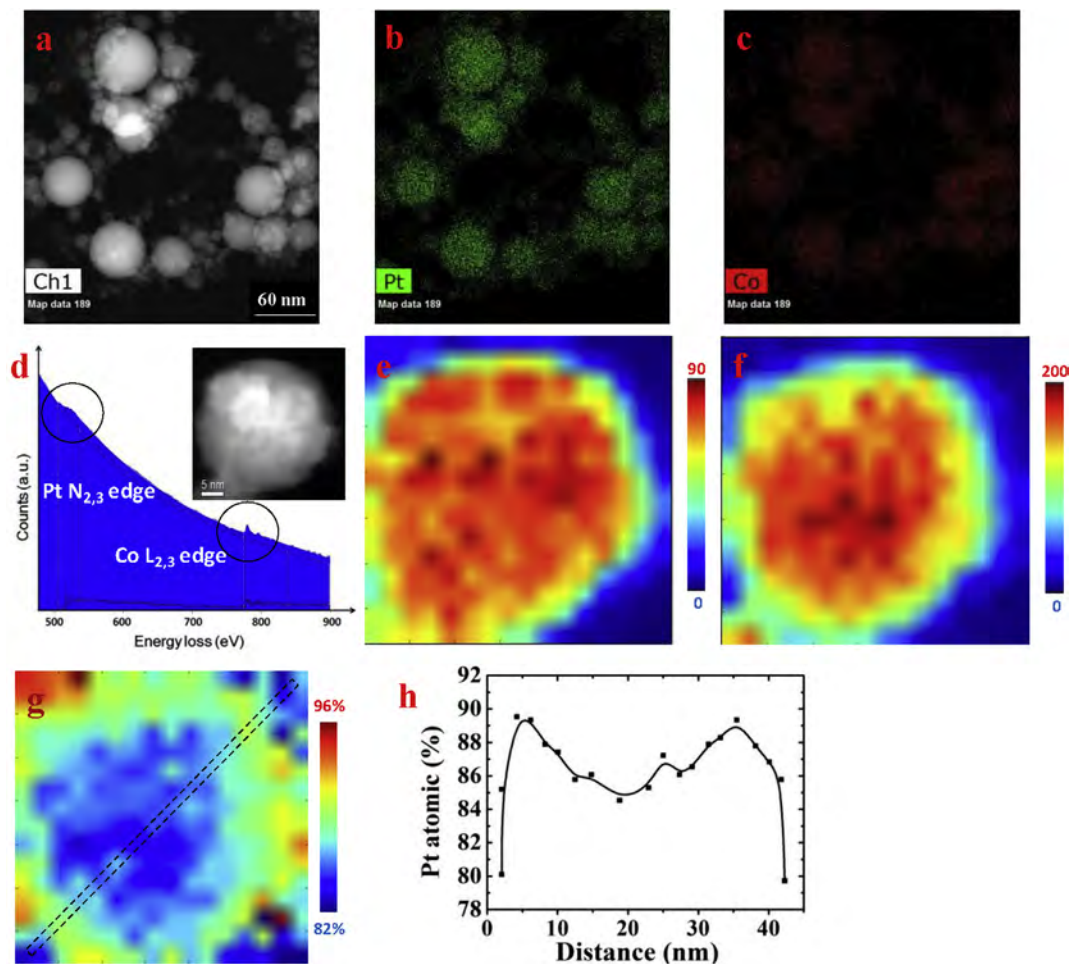
Fig. 3. EDX (**a-c**) and EELS elemental mapping results (**d-h**) for PtCo-2 sample showing: **a.** HAADF-STEM image; **b,c.** EDX mapping of Pt and Co for a on a large scale; **d.** EELS spectrum of a single particle shown in inset; **e, f.** EELS mapping of the corresponding Pt and Co; **g.** EELS mapping indicating Pt/Co atomic ratio from **e** and **f**; **h**. Pt atomic ratio (%) distribution across the line scan across shown as the dashed line in **g**.

Table 1
Summary of degree of alloying for various PtCo NAs through LASiS-GRR.

	K$_2$PtCl$_4$ C (mg/l)	Co ratio % (ICP-OES)	2θ (111)	Crystallite size (nm)	a (Å)	x	Degree of alloying (%)
pH 3	250	6.4	39.81	17.98	3.919	0.03	44.77
pH 7	125	20.6	40.20	3.16	3.882	0.12	53.33
	250	22.1	40.29	4.70	3.874	0.14	58.01
	375	19.9	40.13	9.00	3.889	0.10	46.57
	500	15.5	40.05	10.06	3.896	0.09	51.70
pH 11	250	38.1	40.85	4.15	3.828	0.26	55.96

to the larger degree of coalescence/Ostwald ripening among the seeding PtCo NPs due to faster reduction rates of the K$_2$PtCl$_4$ salt by the seeding Co NPs [56]. The alloying of Co into Pt is demonstrated by the clear shift of PtCo characteristic peaks to higher angles in the XRD patterns in Fig. 2, when compared to the corresponding 2θ values for pure Pt peaks. Specifically, the Pt (111) peak shifts from 39.8° for pure Pt to 40.20°, 40.29°, 40.13° and 40.05° for PtCo-1, PtCo-2, PtCo-3 and PtCo-4 NAs respectively is in accordance with the evolution of Co atomic ratios (%) of 20.6, 22.1, 19.9 and 15.5 in the respective alloys, as calculated from ICP-OES measurements (shown in Table 1). Table 1 also summarizes the values of Co atomic fractions in the alloys (x) and the ratio of alloyed Co (forming Pt$_3$Co) to total Co (Co$_{al}$/Co$_{tot}$), as calculated from Vegard's law and ICP-OES measurement (details in the method section). These calculations

reveal the alloying degrees to vary from ~44% to ~58% for the aforementioned respective PtCo NAs synthesized. Besides, the high resolution TEM image in Fig. S3 (top) indicates the surface facets of the specific PtCo-2 particle are dominated by the PtCo (111) that is well-known for its lower oxygen binding energy and hence, higher ORR activity [30,58,59].

In an effort to further investigate the elemental distributions within the NAs from large-scale as well as detailed elemental mappings respectively, both energy dispersive X-ray spectroscopy (EDX) and electron energy loss spectroscopy (EELS) measurements are shown in Fig. 3 for the PtCo-2 sample. The EDX mapping results in Fig. 3a–c reveal that both Pt and Co are uniformly distributed in all the NPs. Fig. 3d shows a representative EELS spectrum taken from a single NP (shown in the inset), where the two groups of

peaks with onsets located at ~519 and 779 eV are ascribed to the Pt−$N_{2,3}$ and the Co-$L_{2,3}$ edges respectively. The corresponding Pt and Co EELS mapping for this particle are exhibited in Fig. 3e and f, where the Pt distribution area (Fig. 3e) is found to be slightly larger than that for Co (Fig. 3f). For better comparison, the Pt:Co ratio mapping along with a representative line scan across the particle is shown in Fig. 3g, and the corresponding Pt atomic (%) distribution across this line scan is shown in Fig. 3h. These results reveal a thin Pt-rich layer (c.a. a few nanometers) as the particle shell wherein the Co (%) increases gradually towards inner layers. In contrast, the center of the NP bears a relatively uniform but lower Pt:Co ratio (Pt:Co = ~4.5:1). Here it needs to be mentioned that in spite of the higher accuracy of the EELS technique, the inclusion of other signals (e.g. O−K edge at 532 eV) and random noises in the broad Pt−$N_{2,3}$ peak from EELS data can contribute to the slightly higher value of the Pt:Co ratios as calculated from EELS measurements, when compared to that from EDX/ICP-OES quantifications.

3.1.2. PtCo NAs synthesized with different pH conditions

For investigating the impact of the solution phase [H^+] on the structure and composition of the resultant NAs, similar experiments were carried out at pH3 and pH11 conditions respectively (with initial [K_2PtCl_4] of 250 mg/l, and ablation time of 7 min) followed by HCl treatment at pH2 conditions. The PtCo NAs synthesized at pH3 show a much larger mean crystallite size (~17.98 nm) as compared to those at pH11 condition (~4.15 nm). The EDX mappings and spectra also indicate that Co molar ratio in the NA products rises up with the solution phase pH (namely from pH3, pH7 to pH11), as discussed in details in the supporting information along with corresponding TEM images in Fig. S6 and Table 1. It needs to be mentioned that under pH11 conditions, the Pt^{2+} transforms into $Pt(OH)_2$ that eventually precipitates as $PtCl_2$ (see XRD result in Fig. S8) thereby reducing both Pt formation and agglomeration. In this case, as discussed in supporting information, addition of saturated NaCl solution followed by centrifugation for two times helped remove the unwanted $PtCl_2$ salts. The ICP-OES results also support the EDX data wherein the three Co molar ratios for pH3, pH7 and pH11 cases are found to be 6.4%, 22.1% and 38.1% respectively (Table 1). Furthermore, the XRD profiles (Fig. 4) indicate negligible shift in 2θ value (39.81°) for the characteristic PtCo (111) peak in the pH3 sample as compared to the remarkable

positive shift (40.85°) in 2θ values for the PtCo alloy formed at pH11, that is much higher than those for the PtCo-2 sample (40.29°) as well as for standard Pt_3Co (40.53°) alloys. In such a case Pt_1Co_1 alloy (41.4°) with tetragonal crystalline structure might have been partially formed. The aforementioned results for different and yet, directed alloying under different pH conditions are achieved by controlling the relative concentrations of Pt^{2+}, Co and H^+ in the system, as also discussed in details in the next section. Specifically, in acid condition, majority of the Co NPs undergo direct oxidation by solution phase [H^+], which results in fewer amounts of Co available for Pt^{2+} reduction and even less available for alloying with Pt. On the other hand, at pH11 condition, direct oxidation of Co is to a great extent hindered due to the extremely low [H^+] in solution. As a consequence, large amount of Co take part in GRR with Pt^{2+} and in turn alloying with Pt, thereby leading to a much higher Co_{al} in the final products.

3.2. Investigation of ORR electrocatalytic activities

The ORR catalytic activities for the PtCo NAs synthesized with various initial [Pt^{2+}], as investigated with RDE measurements in 0.1 M $HClO_4$ electrolyte solutions, are summarized in Fig. 5. Cyclic voltammetry (CV) scans were conducted from 0.05 to 1.02 V vs. RHE at a scan rate of 50 mV/s. The ECSA calculated from the integration of the hydrogen evolution area in the CV curve indicate a gradual decrease from PtCo-1 to PtCo-4 (i.e., 30.92, 24.25, 18.31 and 14.55 m^2/g respectively), as shown in Fig. 5a and Table 1. This is mainly attributed to the decreasing surface to volume ratios with increasing particle sizes of the PtCo NAs resulting from LASiS-GRR with higher initial [Pt^{2+}]. Fig. 5b provides the ORR polarization curves scanned in O_2-saturated 0.1 M $HClO_4$ electrolyte for the PtCo catalysts under study. The half-wave potential values in Fig. 5b indicate that most of the as-synthesized NA samples, i.e., PtCo-1, PtCo-2 and PtCo-3 outperform the catalytic activities of commercial Pt/C (see Table 2). The best ORR performance is noted for PtCo-2 sample with a 32 mV positive shift in the half-wave potential as compared to the Pt/C sample. This is mainly due to higher Co ratios with good alloying degree (58.01%) in the PtCo-2 sample that shrinks the lattice constant and lowers d-band center which in turn reduces the oxygen binding energy. Added to this, the small particle sizes (mean crystallite size of 4.7 nm in Table 1) with moderate coalescence in PtCo-2 promote catalytic activities due to higher surface to volume ratios. In contrast, the PtCo-4 alloy exhibits the lowest activity, which can be ascribed to its lowest Co ratio (15.5%), poor alloying (51.7%) and largest size (~10 nm) as seen from Table 1. Interestingly, the PtCo-1 sample with smallest mean sizes (~3 nm) and slightly lower alloying degree (53.33%) than PtCo-2 (58%), exhibit less activity. This could be primarily attributed to the excess agglomeration in PtCo-1 (see Fig. 3a). Besides, the diffusion-limited current at high overpotential regions (+0.1 to +0.80 V vs. RHE) reaches ~5.6 mA/cm^2 for all samples, thereby indicating minimal formation of H_2O_2 during the ORR process as well as good charge transfer rates. It is noted that this diffusion-limited current value agrees extremely well with those reported for commercial Pt/C and other peer research works [16,60]. The dynamics of the electron transfer process during ORR were analyzed using the Koutecky−Levich (KL) equation in rotating disk voltammetry (RDV) measurements carried out at different rotation rates (400−2200 rpm), as indicated in the experimental section. Fig. 5c shows the slopes of the KL plots generated from the RDV curves (inset) for the PtCo-2 in the range of 0.70−0.87 V. The slopes estimate the number of transferred electrons (n) to be ~4.0, thereby indicating an ideal four-electron transport process for ORR. Fig. 5d illustrates the Tafel plots extracted from the ORR polarization curves in the mixed kinetic/diffusion regions (low overpotential regions). The calculated
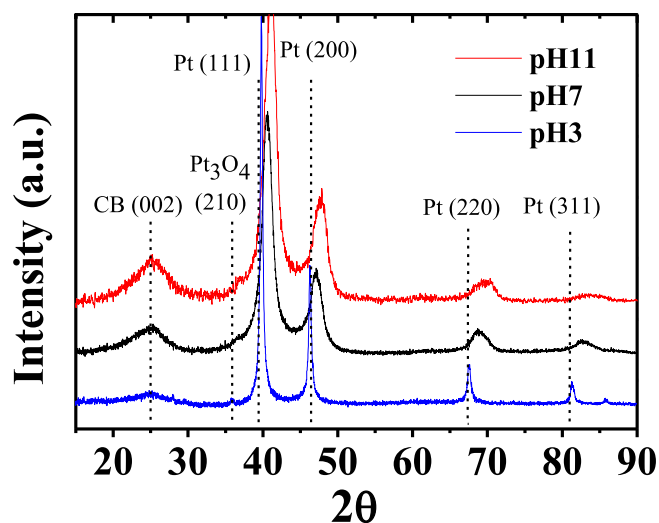
Fig. 4. XRD patterns for PtCo NAs at different pH conditions with same initial K_2PtCl_4 concentration and ablation time (250 mg/l & 7 min respectively). The dash lines mark the standard peak positions for each species.
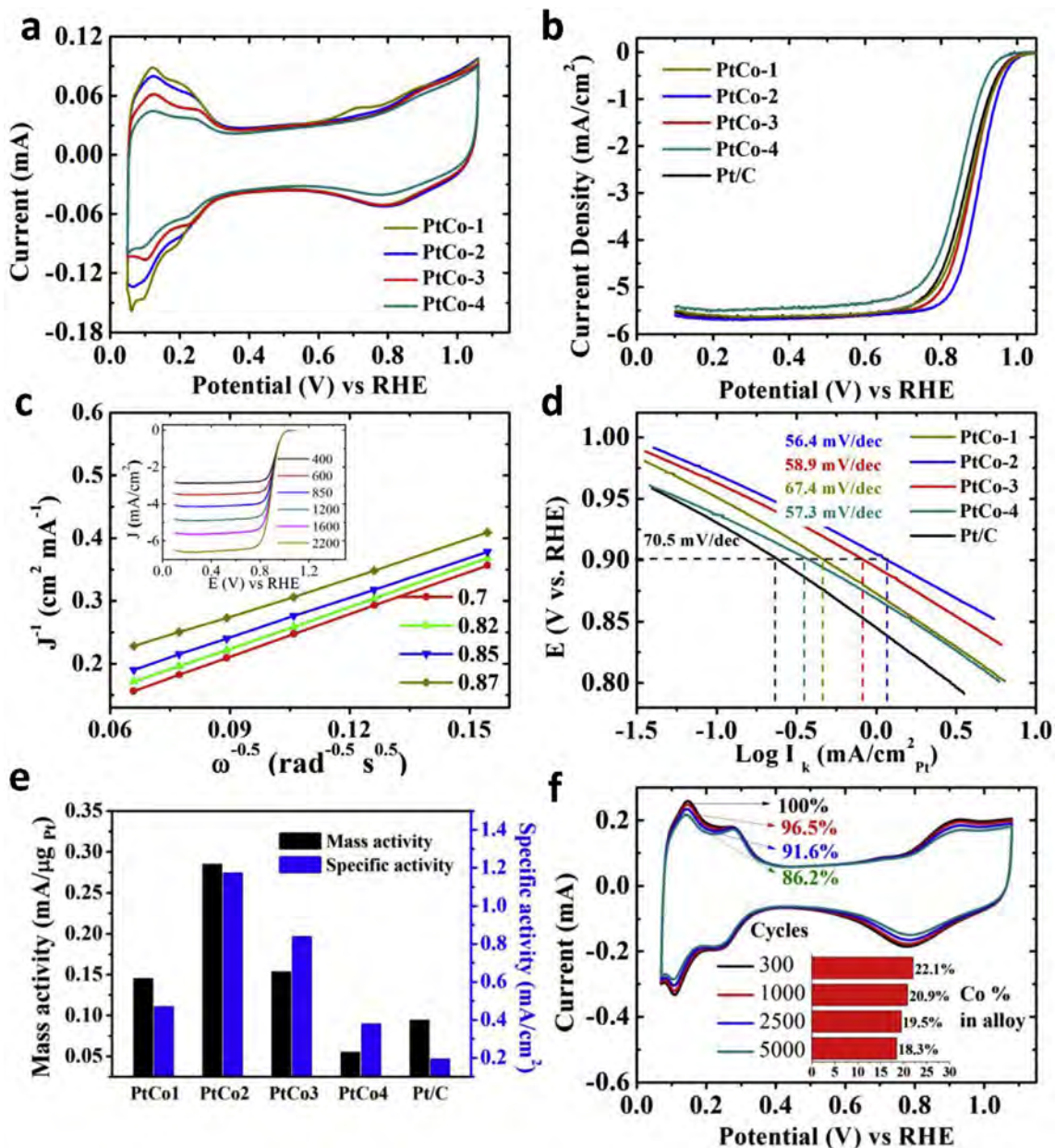
Fig. 5. Electrochemistry data indicating ORR activities of PtCo NAs made via LASiS-GRR when compared to commercial Pt/C samples using: **a.** Cyclic voltammetry curves at a scan rate of 50 mV/S; **b.** Linear sweep voltammograms for ORR polarization curves in 0.1 M HClO₄ electrolyte saturated with dissolved O₂ at 1600 rpm and scan rate of 5 mV/s; **c.** Koutecky−Levich plots from rotating disk voltammogram (RDV) data (shown in inset) for PtCo-2 at different potentials (0.70−0.87 V) indicating four electron transport process for ORR; **d.** Corresponding Tafel plots; **e.** Comparison of mass activity and specific activity at 0.9 V vs. RHE; **f.** Cyclic voltammetry curves indicating the % ECSA values and Co ratio (%) in the alloy after various numbers of potential cycles at a scan rate of 100 mV/s.

Table 2
Summary of electrochemistry test results.

	Pt loading (µg/cm2)	ECSA (m2/g)	I_k at 0.9 V (mA/cm2)	MA (A/mg)	SA (mA/cm2)	Half-wave E (mV vs. RHE)
PtCo-1	19.85	30.92	2.89	0.15	0.47	875
PtCo-2	19.48	24.25	5.55	0.28	1.18	899
PtCo-3	20.03	18.31	3.08	0.15	0.84	879
PtCo-4	21.13	14.55	1.17	0.06	0.38	847
Pt	25.00	48.50	2.36	0.09	0.19	867
pH 3	23.40	6.67	0.62	0.03	0.40	806
pH 11	15.48	44.50	3.65	0.24	0.53	875

Tafel slopes for the PtCo samples are in the range from 56.4 to 67.4 mV/dec, which are lower than the corresponding values for commercial Pt/C (70.5 mV/dec), indicating better charge carrier mobility. Besides, upon comparing the specific activities (SA) for

each of the samples at 0.9 V vs. RHE potential on the Tafel plots in Fig. 5d, all the PtCo samples are found to indicate higher SA values than the Pt/C sample. The detailed mass activity (MA) and SA values at 0.9 V vs. RHE are shown in Fig. 5e and Table 1. The PtCo-2 sample is found to indicate the best catalytic activity with the MA and SA values of 0.28 mA/μg_{Pt} and 1.18 mA/cm^2 respectively, thereby indicating c.a. 3 and 6-fold increase over the corresponding values for Pt/C (0.09 mA/μg_{Pt} and 0.19 mA/cm^2). The outstanding ORR activities for the PtCo NAs is attributed to the uniform NAs with the Pt-rich shell, as evident from the EELS ratio mapping in Fig. 3g & h. Added to this, the absence of any additional chemical including reducing agent/surfactant/stabilization agent during the LASiS-GRR synthesis process eliminates the possibilities of deteriorating the active surface area, thereby benefiting the catalytic performance. Finally, stability tests were conducted for the PtCo-2 sample by scanning CV at the same range as earlier CV tests for 5000 cycles at 100 mV/s. The results shown in Fig. 5f reveal a ~14% decrease in ECSA (from 100% (black) to 86.2% (green) case) after 5000 cycles, while the Co$_{al}$ also diminishes from 22.1% to 18.3%. This is ascribed to the dissolution of catalysts in the acid electrolyte, which is a well-known phenomenon for Pt or other metal based ORR catalysts as also observed in earlier works [4,11,22,30]. Our on-going work is aimed towards addressing this long-standing issue via thermal annealing at high temperature (over 700 °C) for transferring the current disordered Pt$_3$Co to the more stable ordered alloy.

The electrochemistry results for the PtCo NAs synthesized at different pH conditions (referred to as pH3, pH7 and pH11 samples) are summarized in Fig. 6. The pH11 sample exhibits a much higher ECSA (44.50 m^2/g) than the pH7 or PtCo-2 (24.25 m^2/g) and pH3 sample (6.67 m^2/g) as calculated from the hydrogen adsorption peaks in the CV curves (Fig. 6a). This is easily attributed to the

smaller crystallite sizes (~4.15 nm from Table 1) for the pH11 sample as compared to both the pH7 (~4.70 nm) and pH3 (~17.98 nm) samples. For comparing the ORR activities, electrochemistry tests and plots similar to the ones carried out for PtCo-2 samples at pH7 condition are presented in Fig. 6. These measurements include ORR polarization curves (Fig. 6b), Tafel plots (Fig. 6c) and MA/SA comparisons (Fig. 6d). The pH3 sample exhibits the poorest activity as compared to all the other samples, which can be ascribed to its larger crystallite sizes and extremely low Co$_{al}$ (see Table 1). Here the interesting observation is that the pH11 sample, even with higher Co$_{al}$ (~38.1%) and smaller crystallite sizes (~4.15 nm), exhibit slightly less ORR activities in regards to the half-wave potential (~875 V vs. RHE), MA (~0.24 A/mg) and SA (~0.53 mA/cm^2) when compare to the corresponding values for PtCo-2 (namely, 899 V vs. RHE, 0.28 A/mg and 1.18 mA/cm^2). Nevertheless, it needs to be noted that these values are still remarkably better than those for commercial Pt/C (namely, 867 V vs. RHE, 0.09 A/mg and 0.19 mA/cm^2, respectively).

3.3. Reaction pathways for PtCo NA formation: a discussion

In an effort to elucidate the role of LASiS-GRR in tailoring the degree of alloying/composition, structure, and in turn, the ORR activities of the aforementioned PtCo NAs, we dedicate this section towards explaining the detailed mechanistic picture behind the reaction pathways that lead to the formation of various PtCo NAs during LASiS-GRR. The concept of tandem LASiS-GRR is built on the ability to control the various reduction reaction pathways via GRR at the plasma cavitation–liquid interface that are essentially initiated by the rate-limiting source production of Co NPs via LASiS. In doing so, we tune the amount of reduced Pt NPs that alloy with the
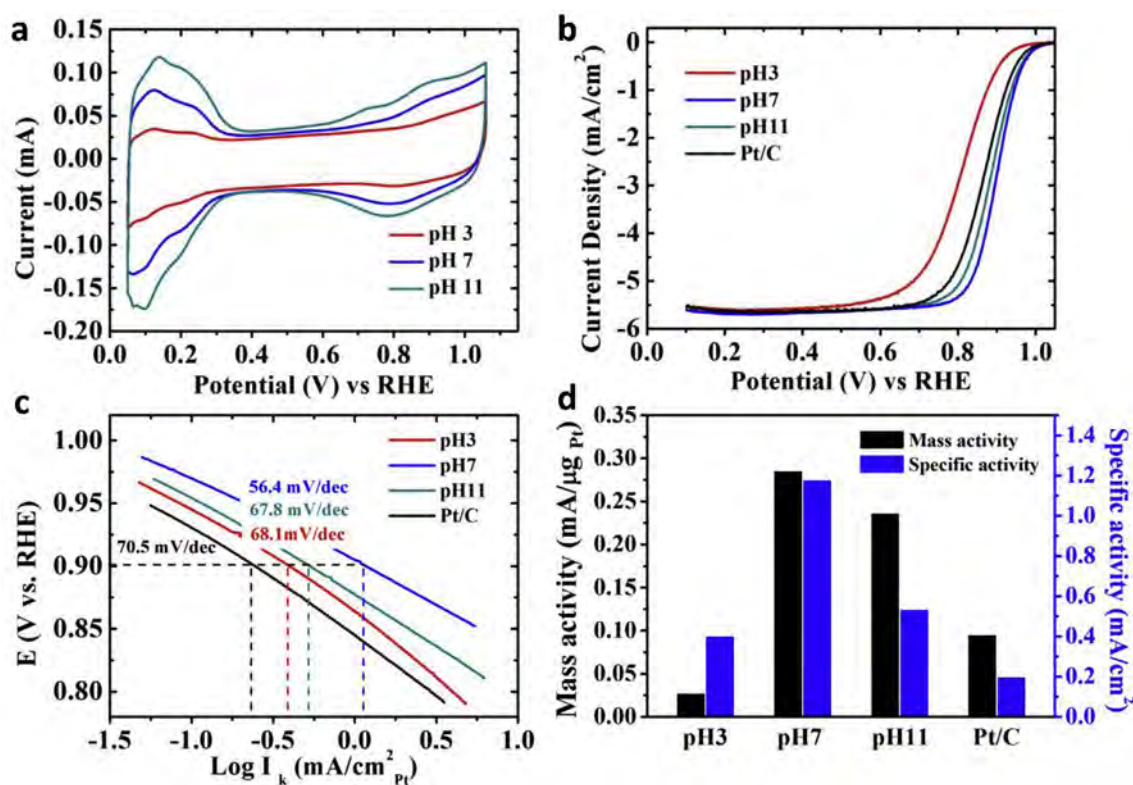
Fig. 6. Electrochemistry data for PtCo NAs made from LASiS-GRR at different pH conditions: **a.** Cyclic voltametry curves at a scan rate of 50 mV/S; **b.** Linear sweep voltammograms for ORR analysis in 0.1 M HClO$_4$ electrolyte saturated with dissolved O$_2$ at 1600 rpm and scan rate of 5 mV/s; **c.** The corresponding Tafel plots; **d.** Comparison of mass activity and specific activity at 0.9 V vs. RHE.

seeding Co NPs, thereby tailoring the composition, structure and degree of alloying in the resulting NA samples. Thus, different extents of alloying in the aforementioned PtCo NAs and in turn their catalytic properties are systematically controlled in a simple yet, elegant fashion by tuning the relative rates of the following reaction mechanisms and pathways, as illustrated in the schematic in Fig. 7 for different initial Pt^{2+} and H^+ (pH conditions) concentrations. In O_2-free solution, the pulsed laser produces seeding Co NPs within the cavitation bubble that undergo the following reactions at the bubble–liquid interface during collisional quenching:

to a much faster reaction 1 than the other two reactions, therefore leaving few Co to alloy with large amount of reduced Pt and hindering the alloying process. To this end, an optimal amount of initial $[Pt^{2+}]$ is expected to produce the largest alloyed Co (Co_{al}).

Meanwhile, the Pt–Co alloying process is also controlled by tuning the solution phase $[H^+]$ or pH conditions. Specifically, in acid conditions (low pH), an extremely low Co_{al} is expected since majority of the seeding Co NPs go through reaction 2 leaving few Co for reaction 3, which is similar to the case with low $[Pt^{2+}]$ at neutral condition. On the other hand, in alkaline conditions (high pH) with
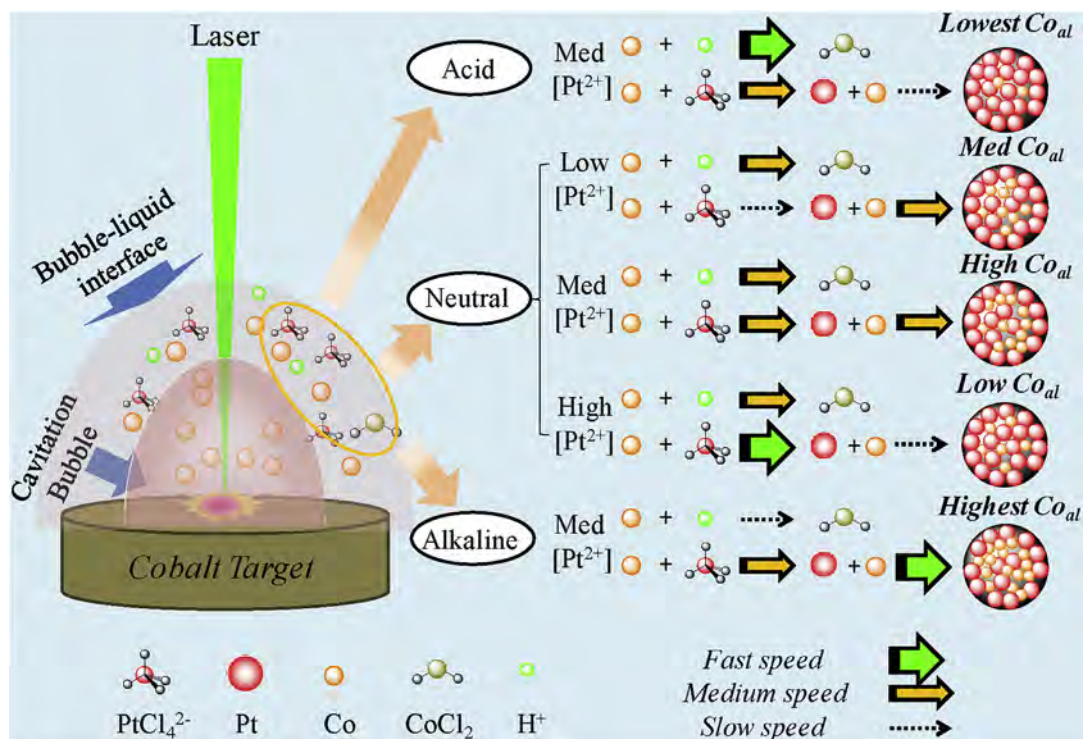
Fig. 7. Schematic diagram indicating the formation of PtCo NAs via tandem LASiS-GRR using different initial Pt^{2+}concentrations and pH conditions; pulsed laser produces seeding Co NPs which expand with the cavitation bubble and react with either Pt^{2+}, H^+ or reduced Pt (alloying process) at the bubble–liquid interface during collisional quenching. Based on the different Pt^{2+} concentration (low, medium, high) and pH conditions (acid, neutral, alkaline), different degrees of alloying for Coal are obtained.

1. Galvanic replacement reaction (GRR) with K_2PtCl_4 based on the respective redox potentials for Co/Co^{2+} (−0.28 V vs. SHE) and Pt^{2+}/Pt (0.76 V vs. SHE):

$$Pt^{2+} + Co \rightarrow Pt + Co^{2+} \qquad (1)$$

2. Oxidation by H^+ ions driven by pH:

$$Co + 2H^+ = Co^{2+} + H_2 \qquad (2)$$

3. Alloying with reduced Pt from Reaction 1:

$$Co + Pt = PtCo(alloy) \qquad (3)$$

At neutral conditions (pH = 7), with same Co production rate from the rate limiting steps of LASiS, the initial $[Pt^{2+}]$ plays a crucial role in driving the rate determining steps of reactions 1 through 3 to finally control the nanostructures and compositions. Specifically, when the initial $[Pt^{2+}]$ is low, the reduction rate of Pt through GRR (reaction 1) is much slower than the direct oxidation of Co by H^+ (reaction 2), therefore the alloying rate between reduced Pt and Co (reaction 3) is also slow. On the other hand, high initial $[Pt^{2+}]$ leads

medium $[Pt^{2+}]$, abundant Co are present for reaction 3, in which case the highest Co_{al} is obtained. The aforementioned reaction mechanisms are also schematically represented in Fig. 7 for different $[Pt^{2+}]$ concentrations (low, medium, high), pH conditions (acid, neutral, alkaline) and corresponding relative speeds of the reaction pathways, namely, fast (big, bold green), medium (bold orange) and slow (dotted black).

To sum it up, the modified LASiS-GRR technique provides an elegant route for synthesizing PtCo NAs with unique nanostructures as well as controllable sizes, Pt:Co ratios and degrees of alloying. Rational tuning of experimental parameters in this facile, green technique allows for clear elucidation of relationships between structure, composition and catalytic performances of specific kinds of alloys (PtCo). In future, we are trying to apply this technique to a more universal alloy system along with efforts directed towards mass production by using different types of laser (pulsed/continuous laser, different laser energy, wavelength, duration time, etc.) and a continuous supply of metal salts through the injection unit in the designed multifunctional cell (Fig. S1). As a result, a green, facile and yet efficient synthesis technique for the mass production of various metal alloys with

controllable physic-chemical and catalytic properties are expected to be realized.

4. Conclusions

In this paper, we report LASiS-GRR as a green, facile synthesis technique for the manufacturing of PtCo NAs as excellent ORR catalysts with controllable size, atomic compositions and alloying degrees. Specifically, the PtCo NAs with crystallite sizes of ~4.70 nm and ~58% degree of alloying (~22% reduction in Pt atomic content) exhibit superior ORR activities in acid electrolyte solutions as compared to the corresponding activities for standard Pt/C catalysts. Such activities are attributed to the unique capabilities of tandem LASiS-GRR to synthesize the aforementioned NAs with controlled sizes and uniform elemental distributions. Specifically, detailed structural characterizations of the NAs from EDX and EELS ratio mappings indicate a thin layer of Pt-rich shell on an alloyed core with relatively uniform Pt:Co ratio. The rational tuning of such structure-property relations are achieved by systematically controlling the initial Pt salt concentrations, ablation times and solution phase pH conditions during the LASiS-GRR technique. The transformative concept here is the ability of seeding NPs generated by the rate limiting step of LASiS to drive the simple redox chemistry in the rate controlling step of GRR that allows directed tailoring of sizes, structures and alloying/compositions in the final NCs/NAs. When operated in tandem, reaction pathways emerging from high-energy liquid-confined plasma can be regulated to create heteronanostructures with metastable structures and phases without the use of any external chemical agents/surfactants.

Acknowledgments

Appendix A. Supplementary data

Supplementary data related to this article can be found at http://dx.doi.org/10.1016/j.jpowsour.2015.11.078.

References

[1] E. Antolini, J.R.C. Salgado, M.J. Giz, E.R. Gonzalez, Effects of geometric and electronic factors on ORR activity of carbon supported Pt-Co electrocatalysts in PEM fuel cells, Int. J. Hydrog. Energy 30 (2005) 1213—1220, http://dx.doi.org/10.1016/j.ijhydene.2005.05.001.

[2] F. Godínez-Salomón, M. Hallen-López, O. Solorza-Feria, Enhanced electroactivity for the oxygen reduction on Ni@Pt core-shell nanocatalysts, Int. J. Hydrog. Energy 37 (2012) 14902—14910, http://dx.doi.org/10.1016/j.ijhydene.2012.01.157.

[3] J.-H. Jang, E. Lee, J. Park, G. Kim, S. Hong, Y.-U. Kwon, Rational syntheses of core-shell Fex@Pt nanoparticles for the study of electrocatalytic oxygen reduction reaction, Sci. Rep. 3 (2013) 2872, http://dx.doi.org/10.1038/srep02872.

[4] S. Koh, M.F. Toney, P. Strasser, Activity-stability relationships of ordered and disordered alloy phases of Pt3Co electrocatalysts for the oxygen reduction reaction (ORR), Electrochim. Acta 52 (2007) 2765—2774, http://dx.doi.org/10.1016/j.electacta.2006.08.039.

[5] X. Li, H.R. Colon-Mercado, G. Wu, J.-W. Lee, B.N. Popov, Development of method for synthesis of Pt—Co cathode catalysts for PEM fuel cells, Electrochem. Solid State Lett. 10 (2007) B201, http://dx.doi.org/10.1149/1.2777009.

[6] Y.-J. Wang, N. Zhao, B. Fang, H. Li, X.T. Bi, H. Wang, Carbon-supported Pt-based alloy electrocatalysts for the oxygen reduction reaction in polymer electrolyte membrane fuel cells: particle size, shape, and composition manipulation and their impact to activity, Chem. Rev. (2015), http://dx.doi.org/10.1021/cr500519c, 150414100746000.

[7] X. Zhao, S. Chen, Z. Fang, J. Ding, W. Sang, Y. Wang, et al., Octahedral Pd@Pt 1.8 Ni core—shell nanocrystals with ultrathin PtNi alloy shells as active catalysts for oxygen reduction reaction, J. Am. Chem. Soc. 137 (2015) 2804—2807, http://dx.doi.org/10.1021/ja511596c.

[8] C. Zhang, S.Y. Hwang, A. Trout, Z. Peng, Solid-state chemistry-enabled scalable production of octahedral Pt-Ni alloy electrocatalyst for oxygen reduction reaction, J. Am. Chem. Soc. 136 (2014) 7805—7808, http://dx.doi.org/10.1021/ja501293x.

[9] Q.-H. Zhang, W.-H. Yang, H.-H. Wang, M.-Q. Wang, C.-J. Cai, Facile synthesis of platinum alloy nanoparticles with enhanced activity for ethylene glycol electro-oxidation, ECS Electrochem. Lett. 3 (2014) F73—F75, http://dx.doi.org/10.1149/2.0031412eel.

[10] L. Han, P. Cui, H. He, H. Liu, Z. Peng, J. Yang, A seed-mediated approach to the morphology-controlled synthesis of bimetallic copper—platinum alloy nanoparticles with enhanced electrocatalytic performance for the methanol oxidation reaction, J. Power Sources 286 (2015) 488—494, http://dx.doi.org/10.1016/j.jpowsour.2015.04.003.

[11] N.M. Markovic, T.J. Schmidt, V. Stamenkovic, P.N. Ross, Oxygen reduction reaction on Pt and Pt bimetallic surfaces: a selective review, Fuel Cells 1 (2001) 105, http://dx.doi.org/10.1002/1615-6854(200107)1:2<105::aid-fuce105>3.3.co;2—0.

[12] U. Paulus, A. Wokaun, Oxygen reduction on carbon-supported Pt - Ni and Pt - Co alloy catalysts, J. Phys. Chem. B 106 (2002) 4181. http://pubs.acs.org/doi/abs/10.1021/jp013442l.

[13] T. Toda, Enhancement of the electroreduction of oxygen on Pt Alloys with Fe, Ni, and Co, J. Electrochem. Soc. 146 (1999) 3750, http://dx.doi.org/10.1149/1.1392544.

[14] V.R. Stamenkovic, B.S. Mun, M. Arenz, K.J.J. Mayrhofer, C. a Lucas, G. Wang, et al., Trends in electrocatalysis on extended and nanoscale Pt-bimetallic alloy surfaces, Nat. Mater. 6 (2007) 241—247, http://dx.doi.org/10.1038/nmat1840.

[15] J. Greeley, I.E.L. Stephens, a S. Bondarenko, T.P. Johansson, H. a Hansen, T.F. Jaramillo, et al., Alloys of platinum and early transition metals as oxygen reduction electrocatalysts, Nat. Chem. 1 (2009) 552—556, http://dx.doi.org/10.1038/nchem.367.

[16] J. Wu, H. Yang, Platinum-based oxygen reduction electrocatalysts, Acc. Chem. Res. 46 (2013) 1848—1857, http://dx.doi.org/10.1021/ar300359w.

[17] US Department of Energy, Fuel Cell Technical Team Roadmap, June 2013, 2013. http://www1.eere.energy.gov/vehiclesandfuels/pdfs/program/fctt_roadmap_june2013.pdf.

[18] B. Chen, D. Cheng, J. Zhu, Synthesis of PtCu nanowires in nonaqueous solvent with enhanced activity and stability for oxygen reduction reaction, J. Power Sources 267 (2014) 380—387, http://dx.doi.org/10.1016/j.jpowsour.2014.05.104.

[19] J. Zhang, H. Yang, J. Fang, S. Zou, Synthesis and oxygen reduction activity of shape-controlled Pt(3)Ni nanopolyhedra, Nano Lett. 10 (2010) 638—644, http://dx.doi.org/10.1021/nl903717z.

[20] Z. Zhu, Y. Zhai, S. Dong, Facial synthesis of PtM (M = Fe, Co, Cu, Ni) bimetallic alloy nanosponges and their enhanced catalysis for oxygen reduction reaction, ACS Appl. Mater. Interfaces 6 (2014) 16721—16726, http://dx.doi.org/10.1021/am503689t.

[21] C. Wang, D. Van Der Vliet, K.C. Chang, H. You, D. Strmcnik, J. a Schlueter, et al., Monodisperse Pt3Co nanoparticles as a catalyst for the oxygen reduction reaction: size-dependent activity, J. Phys. Chem. C 113 (2009) 19365—19368, http://dx.doi.org/10.1021/jp908203p.

[22] C. Wang, N.M. Markovic, V.R. Stamenkovic, Advanced platinum alloy electrocatalysts for the oxygen reduction reaction, ACS Catal. 2 (2012) 891—898, http://dx.doi.org/10.1021/cs3000792.

[23] X. Huang, L. Cao, Y. Chen, E. Zhu, Z. Lin, M. Li, et al., High-performance transition metal — doped Pt 3 Ni octahedra for oxygen reduction reaction, Sci. (80- .) 4489 (2014).

[24] L. Gan, C. Cui, M. Heggen, F. Dionigi, S. Rudi, P. Strasser, Element-specific anisotropic growth of shaped platinum alloy nanocrystals, Sci. (80-.) 346 (2014).

[25] Y.-C. Hsieh, Y. Zhang, D. Su, V. Volkov, R. Si, L. Wu, et al., Ordered bilayer ruthenium-platinum core-shell nanoparticles as carbon monoxide-tolerant fuel cell catalysts, Nat. Commun. 4 (2013) 2466, http://dx.doi.org/10.1038/ncomms3466.

[26] J. Li, G. Wang, J. Wang, S. Miao, M. Wei, F. Yang, et al., Architecture of PtFe/C catalyst with high activity and durability for oxygen reduction reaction, Nano Res. 7 (2014) 1519—1527, http://dx.doi.org/10.1007/s12274-014-0513-1.

[27] H. Yano, M. Kataoka, H. Yamashita, H. Uchida, M. Watanabe, Oxygen reduction activity of carbon-supported Pt-M (M = V, Ni, Cr, Co, and Fe) alloys prepared by nanocapsule method, Langmuir 23 (2007) 6438—6445, http://dx.doi.org/10.1021/la070078u.

[28] S. Choi, M. Shao, N. Lu, A. Ruditskiy, H. Peng, J. Park, et al., Synthesis and characterization of Pd @ Pt À Ni Core À shell octahedra with high activity toward oxygen reduction, ACS Nano (2014) 10363—10371, http://dx.doi.org/10.1021/nn5036894.

[29] Q. Huang, H. Yang, Y. Tang, T. Lu, D.L. Akins, Carbon-supported Pt-Co alloy nanoparticles for oxygen reduction reaction, Electrochem. Commun. 8 (2006) 1220—1224, http://dx.doi.org/10.1016/j.elecom.2006.05.027.

[30] D. Wang, H.L. Xin, R. Hovden, H. Wang, Y. Yu, D. a Muller, et al., Structurally ordered intermetallic platinum—cobalt core—shell nanoparticles with enhanced activity and stability as oxygen reduction electrocatalysts, Nat. Mater. 12 (2012) 81—87, http://dx.doi.org/10.1038/nmat3458.

[31] J.R.C. Salgado, E. Antolini, E.R. Gonzalez, Structure and activity of carbon-supported Pt—Co electrocatalysts for oxygen reduction, J. Phys. Chem. B 108 (2004) 17767—17774, http://dx.doi.org/10.1021/jp0486649.

[32] V. Stamenković, T.J. Schmidt, P.N. Ross, N.M. Marković, Surface composition effects in electrocatalysis: kinetics of oxygen reduction on well-defined Pt3Ni and Pt3Co alloy surfaces, J. Phys. Chem. B 106 (2002) 11970—11979, http://dx.doi.org/10.1021/jp021182h.

[33] C. a. Cortés-Escobedo, R.D.G. González-Huerta, A.M. Bolarín-Miró, F. Sánchez de Jesús, Q. Zhu, S.E. Canton, et al., Mechanically activated Pt-Ni and Pt-Co alloys as electrocatalysts in the oxygen reduction reaction, Int. J. Hydrog. Energy 39 (2014) 16722—16730, http://dx.doi.org/10.1016/j.ijhydene.2014.03.025.

[34] J.W. Kim, J.H. Heo, S.J. Hwang, S.J. Yoo, J.H. Jang, J.S. Ha, et al., Effects of stabilizers on the synthesis of Pt3Cox/C electrocatalysts for oxygen reduction, Int. J. Hydrog. Energy 36 (2011) 12088—12095, http://dx.doi.org/10.1016/j.ijhydene.2011.06.137.

[35] H.T. Duong, M. a Rigsby, W. Zhou, A. Wieckowski, Oxygen reduction catalysis of the Pt 3 Co alloy in alkaline and acidic media studied by X-ray photo-electron spectroscopy and electrochemical methods, Evaluation (2007) 13460—13465.

[36] Q. He, S. Mukerjee, Electrocatalysis of oxygen reduction on carbon-supported PtCo catalysts prepared by water-in-oil micro-emulsion, Electrochim. Acta 55 (2010) 1709—1719, http://dx.doi.org/10.1016/j.electacta.2009.10.054.

[37] B.J. Hwang, S. Murugesan, S. Kumar, C. Chen, M. Cheng, D. Liu, et al., An investigation of − for Pt − Co/C bimetallic nanoparticles toward the oxygen reduction reaction, J. Phys. Chem. C (2007) 15267—15276.

[38] S.C. Zignani, E. Antolini, E.R. Gonzalez, Evaluation of the stability and durability of Pt and Pt-Co/C catalysts for polymer electrolyte membrane fuel cells, J. Power Sources 182 (2008) 83—90, http://dx.doi.org/10.1016/j.jpowsour.2008.03.061.

[39] M.K. Carpenter, T.E. Moylan, R.S. Kukreja, M.H. Atwan, M.M. Tessema, Sol-vothermal synthesis of platinum alloy nanoparticles for oxygen reduction electrocatalysis, J. Am. Chem. Soc. 134 (2012) 8535—8542, http://dx.doi.org/10.1021/ja300756y.

[40] E.I. Santiago, L.C. Varanda, H.M. Villullas, Carbon-supported Pt-Co catalysts prepared by a modified polyol process as cathodes for PEM fuel cells, J. Phys. Chem. C 111 (2007) 3146—3151, http://dx.doi.org/10.1021/jp0670081.

[41] Z. Liu, C. Yu, I. a. Rusakova, D. Huang, P. Strasser, Synthesis of Pt3Co alloy nanocatalyst via reverse micelle for oxygen reduction reaction in PEMFCs, Top. Catal. 49 (2008) 241—250, http://dx.doi.org/10.1007/s11244-008-9083-2.

[42] N. Kristian, Y. Yu, J.M. Lee, X. Liu, X. Wang, Synthesis and characterization of Cocore-Ptshell electrocatalyst prepared by spontaneous replacement reaction for oxygen reduction reaction, Electrochim. Acta 56 (2010) 1000—1007, http://dx.doi.org/10.1016/j.electacta.2010.09.073.

[43] J.N. Zheng, L.L. He, C. Chen, A.J. Wang, K.F. Ma, J.J. Feng, One-pot synthesis of platinum3cobalt nanoflowers with enhanced oxygen reduction and methanol oxidation, J. Power Sources 268 (2014) 744—751, http://dx.doi.org/10.1016/j.jpowsour.2014.06.109.

[44] J.D. Blakemore, H.B. Gray, J.R. Winkler, A.M. Müller, Co 3 O 4 nanoparticles made by pulsed-laser ablation in liquids as high activity catalysts for water oxidation, ACS Catal. 3 (2013) 2497—2500.

[45] G. Ledoux, D. Amans, C. Dujardin, K. Masenelli-Varlot, Facile and rapid synthesis of highly luminescent nanoparticles via pulsed laser ablation in liquid, Nanotechnology 20 (2009) 445605, http://dx.doi.org/10.1088/0957-4484/20/44/445605.

[46] L. Liao, Q. Zhang, Z. Su, Z. Zhao, Y. Wang, Y. Li, et al., Efficient solar water-splitting using a nanocrystalline CoO photocatalyst, Nat. Nanotechnol. 9 (2014) 69—73, http://dx.doi.org/10.1038/nnano.2013.272.

[47] V. Amendola, M. Meneghetti, Laser ablation synthesis in solution and size manipulation of noble metal nanoparticles, Phys. Chem. Chem. Phys. 11 (2009) 3805—3821, http://dx.doi.org/10.1039/b900654k.

[48] G. Cristoforetti, E. Pitzalis, R. Spiniello, R. Ishak, M. Muniz-Miranda, Production of palladium nanoparticles by pulsed laser ablation in water and their characterization, J. Phys. Chem. C 115 (2011) 5073—5083, http://dx.doi.org/10.1021/jp109281q.

[49] K.Y. Niu, J. Yang, S. a. Kulinich, J. Sun, X.W. Du, Hollow nanoparticles of metal oxides and sulfides: fast preparation via laser ablation in liquid, Langmuir 26 (2010) 16652—16657, http://dx.doi.org/10.1021/la1033146.

[50] V. Amendola, M. Meneghetti, What controls the composition and the structure of nanomaterials generated by laser ablation in liquid solution? Phys. Chem. Chem. Phys. 15 (2012) 3027—3046, http://dx.doi.org/10.1039/c2cp42895d.

[51] P. Liu, W. Cai, M. Fang, Z. Li, H. Zeng, J. Hu, et al., Room temperature synthesized rutile TiO(2) nanoparticles induced by laser ablation in liquid and their photocatalytic activity, Nanotechnology 20 (2009) 285707, http://dx.doi.org/10.1088/0957-4484/20/28/285707.

[52] P. Liu, H. Cui, C.X. Wang, G.W. Yang, From nanocrystal synthesis to functional nanostructure fabrication: laser ablation in liquid, Phys. Chem. Chem. Phys. 12 (2010) 3942—3952, http://dx.doi.org/10.1039/b918759f.

[53] a. Miotello, R. Kelly, Laser-induced phase explosion: new physical problems when a condensed phase approaches the thermodynamic critical temperature, Appl. Phys. A Mater. Sci. Process 69 (1999) 67—73, http://dx.doi.org/10.1007/s003399900296.

[54] S. Barcikowski, G. Compagnini, Advanced nanoparticle generation and excitation by lasers in liquids, Phys. Chem. Chem. Phys. 15 (2013) 3022—3026, http://dx.doi.org/10.1039/c2cp90132c.

[55] P. Wagener, S. Ibrahimkutty, A. Menzel, A. Plech, S. Barcikowski, Dynamics of silver nanoparticle formation and agglomeration inside the cavitation bubble after pulsed laser ablation in liquid, Phys. Chem. Chem. Phys. 15 (2013) 3068—3074, http://dx.doi.org/10.1039/c2cp42592k.

[56] S. Hu, C. Melton, D. Mukherjee, A facile route for the synthesis of nano-structured oxides and hydroxides of cobalt using laser ablation synthesis in solution (LASIS), Phys. Chem. Chem. Phys. 16 (2014) 24034—24044, http://dx.doi.org/10.1039/C4CP03018D.

[57] H. Zeng, X.W. Du, S.C. Singh, S. a Kulinich, S. Yang, J. He, et al., Nanomaterials via laser ablation/irradiation in liquid: a review, Adv. Funct. Mater. 22 (2012) 1333—1353, http://dx.doi.org/10.1002/adfm.201102295.

[58] G. Sievers, S. Mueller, A. Quade, F. Steffen, S. Jakubith, A. Kruth, et al., Meso-porous Pt-Co oxygen reduction reaction (ORR) catalysts for low temperature proton exchange membrane fuel cell synthesized by alternating sputtering, J. Power Sources 268 (2014) 255—260, http://dx.doi.org/10.1016/j.jpowsour.2014.06.013.

[59] A. Schenk, C. Grimmer, M. Perchthaler, S. Weinberger, B. Pichler, C. Heinzl, et al., Platinum-cobalt catalysts for the oxygen reduction reaction in high temperature proton exchange membrane fuel cells − long term behavior under ex-situ and in-situ conditions, J. Power Sources 266 (2014) 313—322, http://dx.doi.org/10.1016/j.jpowsour.2014.05.023.

[60] C. Wang, M. Chi, D. Li, D. Van Der Vliet, G. Wang, Q. Lin, et al., Synthesis of homogeneous Pt-bimetallic nanoparticles as highly efficient electrocatalysts, ACS Catal. 1 (2011) 1355—1359, http://dx.doi.org/10.1021/cs200328z.

[61] S. Hu, G. Goenaga, C. Melton, T. Zawodzinski, D. Mukherjee, PtCo/CoOx Nanocomposites: Bifunctional electrocatalysts for oxygen reduction and evolution reactions synthesized via tandem laser ablation synthesis in solution-galvanic replacement reactions, Appl. Catal. B (Environ.) 182 (2015) 286—296.